Proceedings of the 7th International Conference on Mechanics and Materials in Design
Albufeira/Portugal 11-15 June 2017. Editors J.F. Silva Gomes and S.A. Meguid.
Publ. INEGI/FEUP (2017)

PAPER REF: 6548

DESIGN OF A CRUSHABLE THERMAL PROTECTION SYSTEM FOR THE EARTH RE-ENTRY CAPSULE

João Carvalho[1], Carlos Ribeiro[2], Ricardo Sá[2], Angelo Marques[2], Filipa Carneiro[2], Paulo Chaves[3], Nuno Marques[3], Edgar Carrolo[3], Paulo J. Antunes[4(*)], Júlio C. Viana[4], Denis Rebuffat[5], Ivan Ngan[5]

[1]ACC-Amorim Cork Composites, Mozelos, Portugal
[2]PIEP-Innovation in Polymer Engineering, Guimarães, Portugal
[3]ISQ-Instituto de Soldadura e Qualidade, Lisboa, Portugal
[4]Critical Materials S.A., Caldas das Taipas, Guimarães, Portugal
[5]ESA-European Space Agency, Noordwijk, The Netherlands
[(*)]*Email:* pjantunes@critical-materials.com

ABSTRACT

In this work and in order to design a cTPS-Crushable Thermal Protection system for the ERC-Earth Reentry Capsule, a numerical multiphysics approach was proposed and applied, supported by data obtained from a detailed thermomechanical material characterization plan.

The proposed numerical methodology includes the relevant underlying physics of the ERC re-entry, land impact and post-impact phases. Thus, three numerical simulations procedures were envisaged: 1) a thermal simulation of the ERC re-entry, 2) a dynamic analysis of the impact phase and 3) a post-impact thermal analysis. The output of each phase was used as initial conditions of the subsequent one. The cTPS and ERC conceptual design were validated by these in-depth thermal and structural simulations, which numerically confirmed all the system requirements fulfilling.

Experimental drop-tests and thermal tests were considered and performed in order to check the structural, kinematical and thermal behaviour of the ERC and cTPS solutions proposed and its compliance with the numerical models and mission requirements.

Keywords: crushable plasticity, atmospheric re-entry, ERC, cTPS-Crushable Thermal Protection System.

INTRODUCTION

The MSR and Phootprint (or Phobos Sample Return) mission will return samples from planet Mars and Mars moon Phobos, respectively. These samples will be transported in a bio-container encapsulated in an Earth Re-entry Capsule (ERC) that will perform a hard landing on Earth. The ERC will be released from the Earth Return Vehicle (ERV) and re-enter earth's atmosphere. The re-entry stage will subject the ERC to demanding thermo-mechanical loads.

Through all of the process the ERC will be responsible for ensuring the sample-container is below established levels of temperature and deceleration. Given these requirements, a crushable Thermal Protection System (cTPS) was developed in order to absorb both impact and thermal energy that the ERC will be subjected in the different atmospheric re-entry phases, while ensuring an aerodynamically stable behavior.

BACKGROUND AND OBJECTIVES

Background

Hard landing on earth of an ERC without the use of parachutes or propulsion systems is a very demanding thermomechanical situation for which the selected materials should be thermomechanical compliant with the mechanical and thermal efforts developed during all the re-entry phase.

For the re-entry phase a TPS (Thermal Protection System) material is introduced in the ERC to limit the heat conduction to the cold structure from the ablative layer (NASA, 2017). Also it controls the temperature at the interface with the inner compartment (bio-container and beacons). In the case of passive landing it is needed an interface material that dissipate/absorb the kinetic energy controlling, simultaneously, the bio-container's deceleration and maintaining the thermal conduction as low as possible. One way to control bio-container´s deceleration is the gradual compression of the interface material what could be achieved through the gradual compression of a crushable foam.

A crushable thermal protection system, cTPS, shall perform simultaneously structural and thermal functions, according to the space application. The former requires the capability of: a) absorption of impact energy during landing; b) sustaining dynamic pressure induced loads during re-entry; and c) other mechanical requirements. The thermal function must provide the capability of: a) sustaining the aerothermodynamics heat loads during re-entry; b) keeping the sample canister (or bio-container) at a specified temperature; and, c) other thermal requirements. The crushable TPS system together should be able to protect the bio-container (see Figure 2.1) from high decelerations peaks and extreme temperatures during ERC's re-entry, impact and post-impact phases.

Objectives

The activities are developed under the ESA project: Design of a Crushable TPS for the ERC (TEC-MSS/2011/226/ln/IN) with the principal aim to investigate and design a multifunctional cTPS structure that act as a heat shield for planetary re-entry and brings an adequate impact response during hard landing. Two different ERC's were considered for development. The first ERC is named MSR with an external diameter equal to approximately 1.5m and maximum weight varying in the range [120, 150] kg. For this geometry two types of thermal protection systems materials (varying material's density and thermal properties) named LD-TPS (low density) and HD-TPS (high density) were considered. The Phootprint ERC is a smaller version of the MSR's ERC with 0.75m of external diameter and 30kg in maximum weight.

Below are summarized the main objectives for the project:

1) identify materials and mixed solutions for thermal and structural protection;
2) material characterization for design concept and analysis;
3) set up a conceptual solution for cTPS solution;
4) design and built breadboard models for concept demonstration;
5) reach to the TRL 3 level in the concept design and experimental demonstration;
6) perform experimental tests to verify the proposed cTPS systems.

MAIN REQUIREMENTS AND SPECIFICATIONS

In Fig. 1 is depicted a schematic representation of the ERC where it is visible the cTPS system is composed by: 1) the external TPS layer, 2) the primary structure and 3) a crushable material.

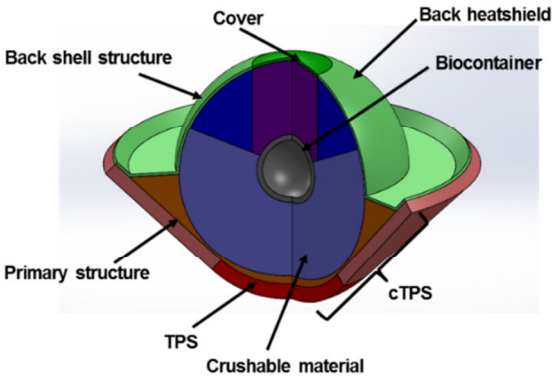

Fig. 1 - A schematic representation of the ERC.

Several requirements were considered for the conceptual design of the ERC. Below, are summarized some of the most important specifications whose compliance is detailed in subsequent sections of this document:

1) Limit deceleration of the bio-container to less than 500.0 g's (2000 g's for Phootprint ERC with 800g's as optimal value), considering an impact velocity of 40.0 m/s with 30º half-cone orientation;
2) The average temperature seen by the bio-container is < 20.0 °C. The post-impact phase duration is 2.0 hours;
3) The in-service temperature range considered for the crushable material is [-20, 170]ºC.

MATERIAL SELECTION AND EXPERIMENTAL TESTS

In this section are outlined the most relevant results obtained during the detailed experimental tests phase concerning the pre-selected materials.

Crushable material pre-selection

After a detailed bibliographic review and preliminary material tests (uniaxial compression and impact tests), three different materials (PMI51 (Evonik, 2016), PM110 (Evonik, 2016) and NL20 (ACC-Amorim Cork Composites, 2016)) were pre-selected as potential materials for use in the ERC. The PMI material correspond to a Rohacell® grade of Polymethacrylimide foam from Evonik Industries, while NL20® is a cork material from ACC-Amorim Cork Composites.

Mechanical and thermal tests data

The detailed material tests procedure compromise the following mechanical and thermal material tests:

- Mechanical Tests
  1) Uniaxial compression (with strain rate and temperature dependence);

2) Tensile loading (with temperature dependence);
3) Impact (with strain rate and temperature dependence);
4) Shear (with temperature dependence);
5) Thermal cycle;
6) COF-Coefficient of friction (static and kinetic);
7) De-pressurization.

- Thermal Tests
  1) Thermal conductivity (with deformation dependence);
  2) Specific heat;
  3) Thermal expansion.

Below is shown the compressive behaviour of PMI51 (WF grade) considering quasi-static (see Fig. 2a) and high strain-rate loading conditions (see Fig. 2b)). In Fig. 2a) it is well evidenced the long stress plateau (yield stress equal to approximately 0.75MPa for room temperature and quasi-static loading conditions) and, simultaneously, the low thermal dependency on mechanical properties evidenced by the PMI51WF foam. The reduced strain-rate sensitivity of PMI51WF is depicted in Fig. 2b) for strain-rates ranging between 500s-1 and 1000s-1.The long and well defined stress plateau together with the magnitude of the yield stress are important factors for the control of bio-container's deceleration peak value.

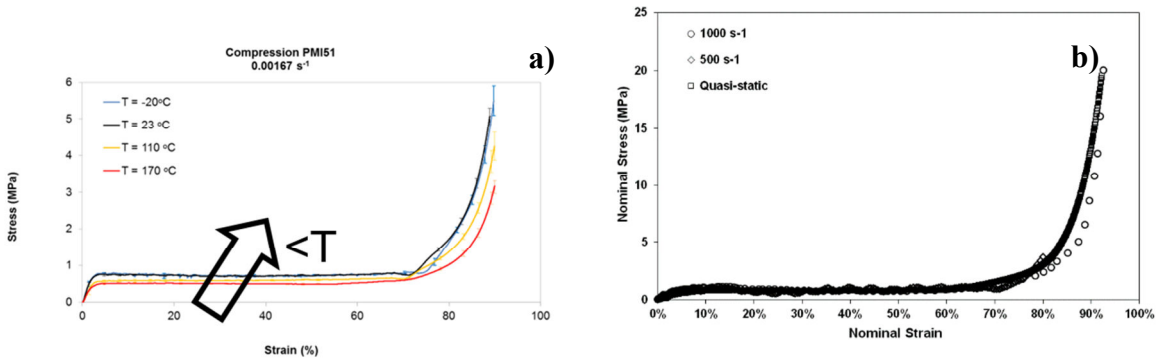

Fig. 2 - Uniaxial compression data for PMI51WF foam considering: a) different temperatures and quasi-static loading conditions ($\dot{\boldsymbol{\varepsilon}}$ = 0.00167s-1) and b) different strain rates and room temperature (T=23ºC).

Fig. 3 depicts the influence of thermal cycling in the mechanical properties of PMI5WF. After 512 thermal cycles in the range [-20, 70] ºC are not visible significant changes on the mechanical response of the material.

The effect of permanent deformation and temperature in the thermal conductivity of PMI51WF is depicted in Fig. 4 where it is notorious the increase of thermal conductivity with the permanent (plastic) deformation level (ε_{pl}) in result of the severe material densification due to the internal collapse of foam's cell structure.

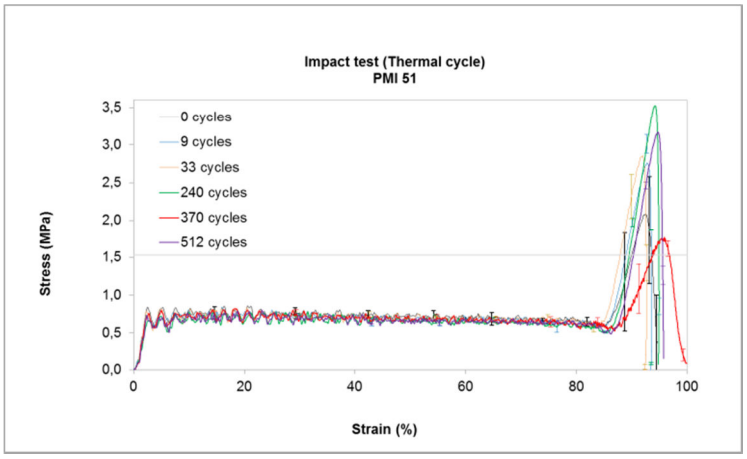

Fig. 3 - Effect of thermal cycling on the mechanical properties (response to impact) of PMI51WF.

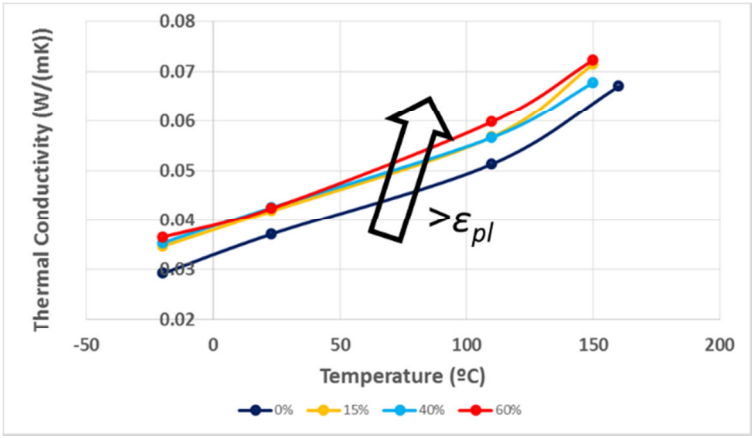

Fig. 4 - Thermal conductivity dependence with plastic (permanent) deformation.

NUMERICAL ANALYSIS

In this section will be highlighted the main aspects of numerical modelling of re-entry phenomena, including a summary of the results for each phase. In this section will be reported the main results obtained for the MSR (LD-TPS case) and Phootprint ERC's.

Numerical modelling workflow

The numerical modelling workflow is summarized in Fig. 5. Three different modelling phases were considered: 1) Re-entry phase; 2) Impact phase and 3) Post-Impact phase.

Geometries, structures and materials

In Fig. 6a) is shown the geometry, and respective materials, considered for the MSR (LD-TPS case) and for the Phootprint's ERC (in Fig. 6b)). Table 1 summarize the materials, and respective mechanical behaviour, considered for the numerical analysis.

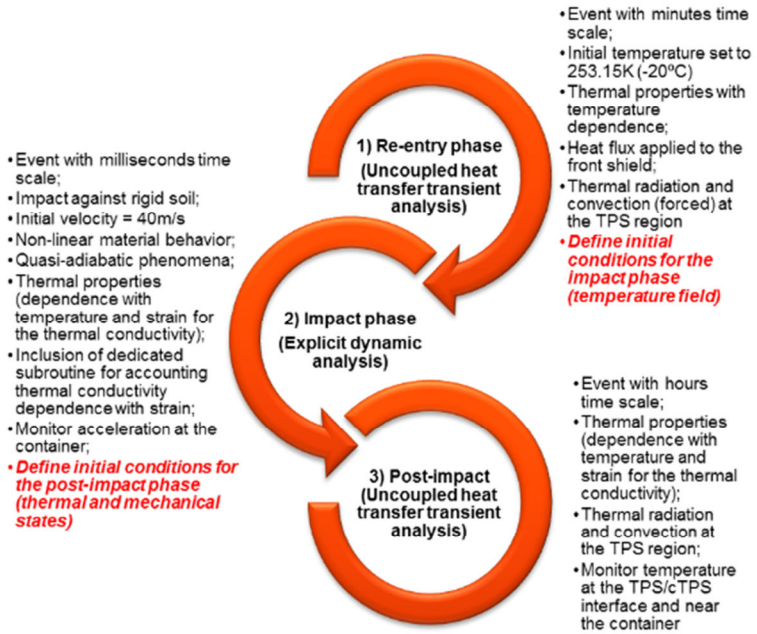

Fig. 5 - Simulation data flow and strategy.

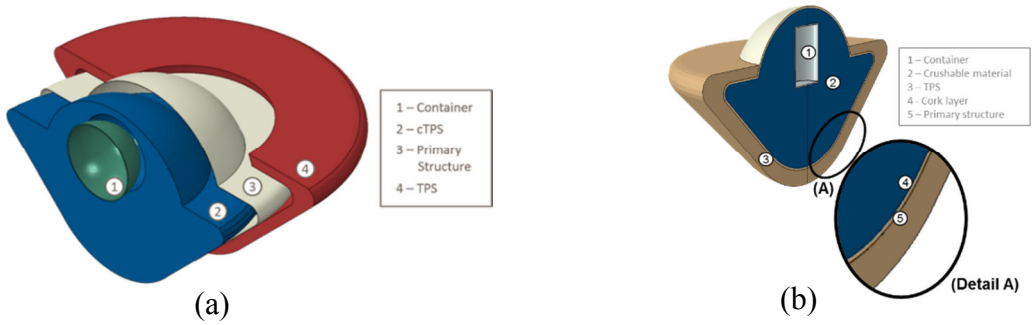

Fig. 6 - ERC's layout for a) MSR and b) Phootprint ERC.

Table 1 - Materials considered and respective material behaviour.

Structure:	**Material**	**Mechanical behavior**	**Temperature dependence**
TPS	PICA like	Elastic (isotropic) (Agrawal & Chavez-Garcia, 2011)	On thermal properties
Crushable material	PMI51WF	Crushable plasticity (Deshpande & Fleck, 2000)	On thermal and mechanical properties
Primary structure	CFRP	Elastic (orthotropic) + Hashin's damage law (Z, 1980)]	On mechanical properties
Biocontainer	Titanium	Fully rigid	N/A
Thermal barrier	Cork (NL20)	Hyperelastic (Hyperfoam N=3)	On thermal and mechanical properties
Soil	Dense sand (sieve 4)	Elastoplastic (Mohr-Coulomb) (Geothecnical Parameters, 2015)	N/A

Loads and boundary conditions

Thermal loads, boundary conditions and thermal interactions considered for the uncoupled thermal analysis (re-entry phase) are seen in Fig. 7a). For the re-entry thermal analysis it was considered both radiation, convection and thermal conduction phenomena. Heat fluxes transients ($\vec{\phi}$) applied to TPS external surface can be seen in Fig. 7b).

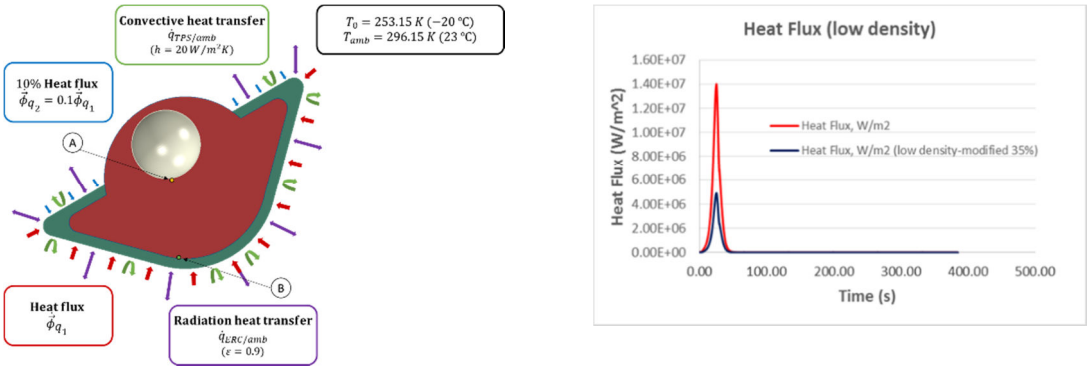

(a) (b)

Fig. 7 - Thermal loads and boundary conditions for MSR ERC in a) and incident heat flux in b).

In Fig. 8 is shown the boundary conditions considered for the impact phase. The velocity vector magnitude was set to 40ms^{-1}, deviated 30º from the normal-to-the-ground. Initial temperature field (T_0) was retrieved from the uncoupled heat transfer analysis relative to the atmospheric re-entry. For the post-impact phase (see Fig. 9), additionally to the thermal boundary and interactions considered for the re-entry phase, both solar radiation and thermal conduction between soil and ERC were considered. Additionally, a dedicated subroutine that account the relation between permanent deformation and thermal conductivity was considered for the uncoupled thermal simulation of the post-impact phase.

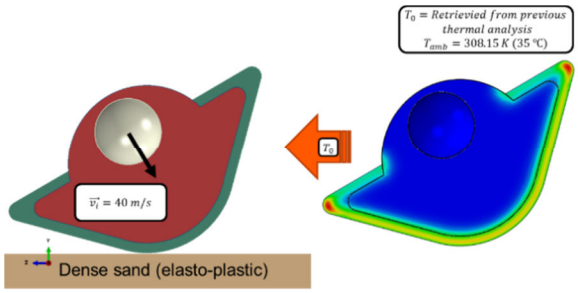

(a)

Fig. 8 - Boundary and kinematic conditions considered for the impact phase.

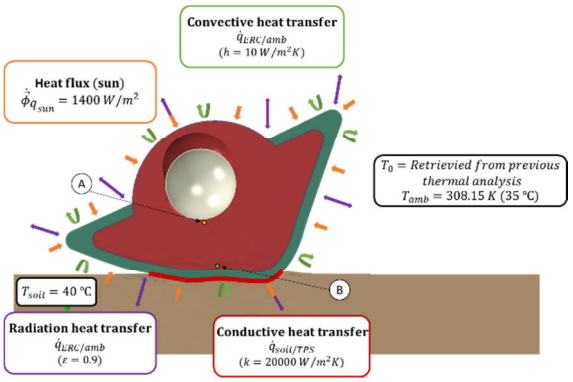

(b)

Fig. 9 - Thermal boundary conditions considered for the post-impact phase

Thermal loads and boundary conditions considered for the Phootprint mission are similar to the ones described above.

RESULTS

The final temperature field at the end of re-entry phase obtained for the MSR (LD-TPS case) can be seen in Fig. 10a). In Fig. 10b) is shown the nodal temperature transient obtained at the crushable material's interface with primary structure (red line) and in a node near the container (blue line).

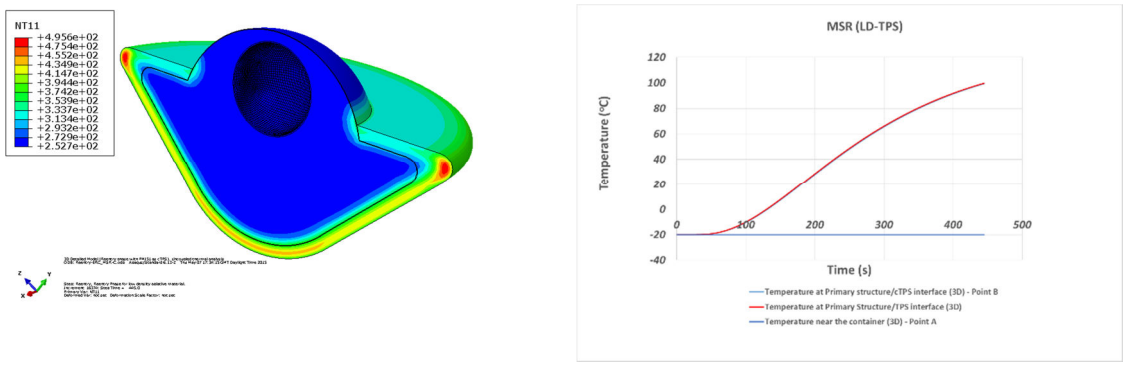

(a) (b)

Fig. 10 - Nodal temperature field (in degrees Kelvin) for: a) the MSR LD-TPS case (cross-section view) and b) temperature transient for a point near the container and at the crushable-material/primary-structure interface.

The deformed configuration of the MSR's ERC (LD-TPS) after impacting a deformable soil at 40ms-1 is shownin Fig. 11a). Deceleration and velocity components (axial-22 and transversal-33) and magnitude, at container's centre-of-mass, is depicted in Fig. 11b).

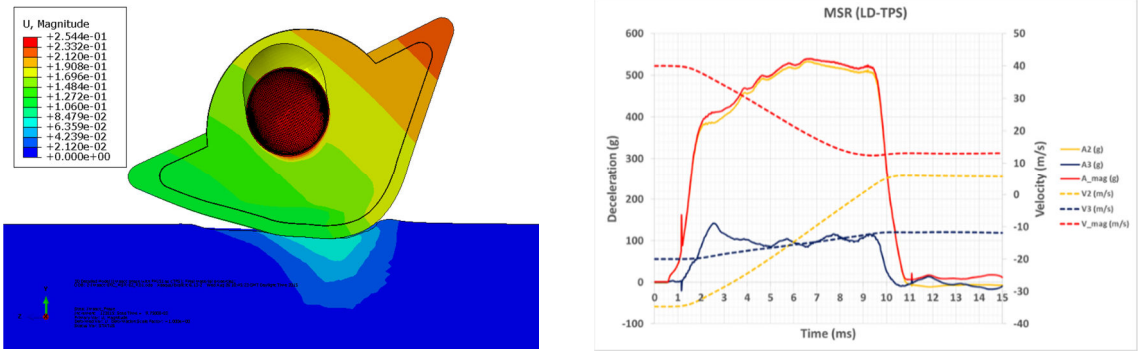

(a) (b)

Fig. 11 - Nodal displacement (in meters) field (at t=10ms) for the MSR LD-TPS case (cross-section view) and b) deceleration and velocity transients, at container's centre-of-mass for MSR ERC's (LD-TPS)

Temperature field obtained after 2h of heat transfer between ERC and atmosphere is shown in Fig. 12a). Thermal transient obtained, for two representative points (near the container-point A and at the interface between crushable material and primary structure-point B), is shown in Fig. 12b). The thermal results found on Fig. 12 consider the influence of material plastic deformation on the thermal conductivity of the crushable foam.

In Fig. 13a) is visualized the three dimensional nodal temperature field (in a cross-section view) at the end of re-entry phase (t=440s). Temperature transients for points A and B and C are displayed in Fig. 13b).

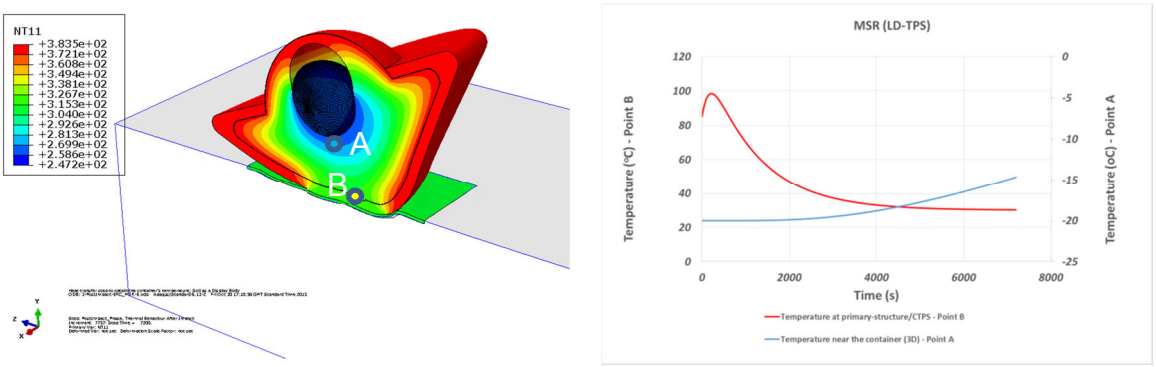

(a) (b)

Fig. 12 - Nodal temperature field for: a) the MSR LD-TPS case (cross-section view) after 2h post-impact and b) temperature transients for points A (blue line) and B (red line) considering the entire duration of the post-impact phase.

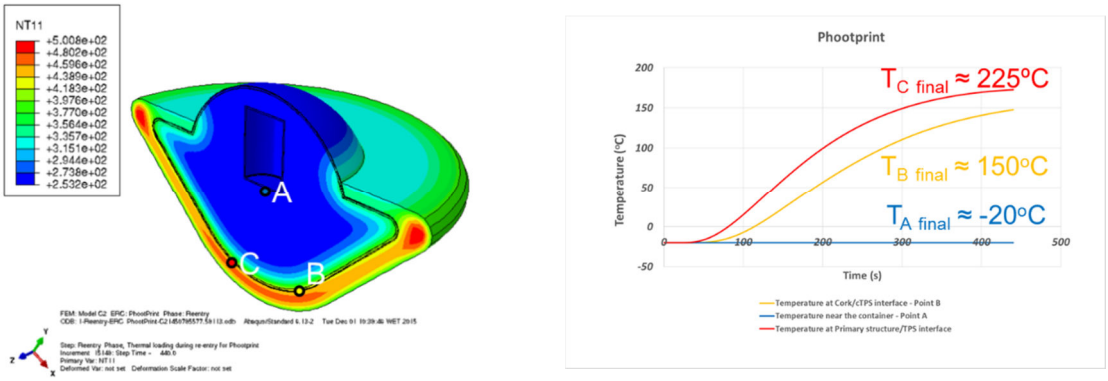

(a) (b)

Fig. 13 - a) Nodal temperature field (in Kelvin) for the Phootprint ERC case (cross-section view) and b) temperature transients for points A, B and at the interface primary-structure/TPS (point C).

The deformed configuration of Photoprint's ERC after impacting a deformable soil at 40ms^{-1} is visiblein Fig. 14a). Deceleration and velocity components (axial-zz and radial-rr for a local cylindrical coordinate system) and the correspondent magnitude, at container's centre-of-mass, is shown in Fig. 14b).

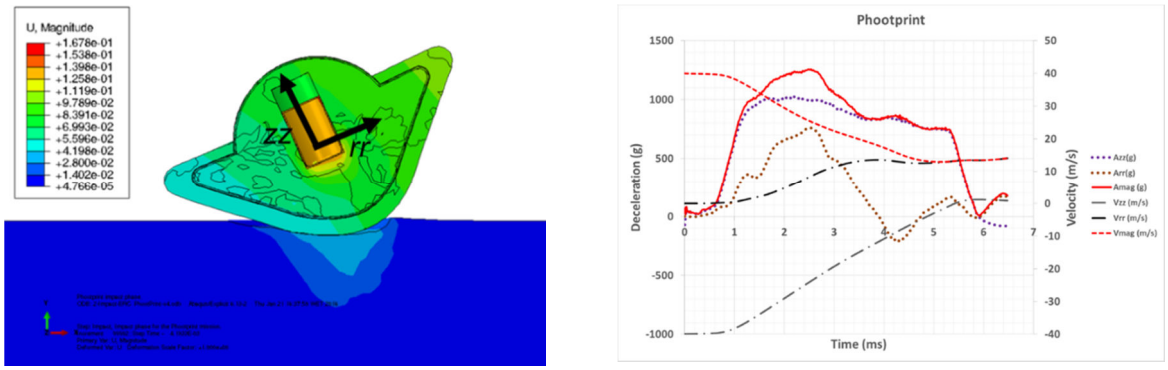

(a) (b)

Fig. 14 - a) Nodal displacement (in meters) field (at t=4.13ms) for the Phootprint case; b) deceleration and

velocity transient (cylindrical coordinates), at container's centre-of-mass.

In Fig. 15a) is shown the nodal temperature field after 7200s (2h) of heat transfer during the post-impact phase. In Fig. 15b) is plotted the temperature transient for point A (near the bio-container) and point B (interface cork/crushable material).

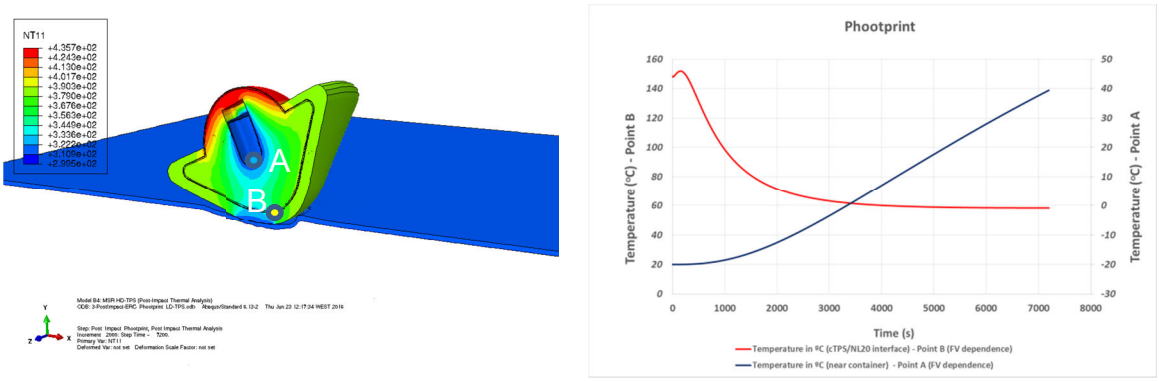

(a) (b)

Fig. 15 - a) Nodal temperature field for the Phootprint case (cross-section view) after 2h post-impact; b) temperature transients for a point near the container (blue line) and at the crushable material interface.

BREADBOARDS AND EXPERIMENTAL PROCEDURE

Breadboards construction

In Fig. 16 and Fig. 17 are shown the full-scale breadboard and the half-scale breadboards, respectively, produced for the experimental tests.

Fig. 16 - Full-scale breadboard demonstrator.

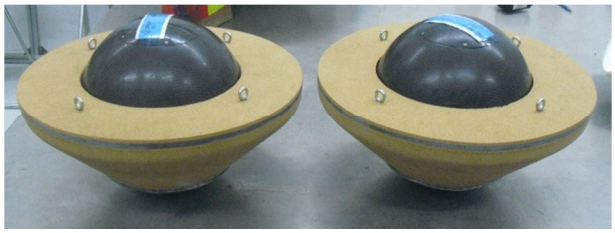

Fig. 17 - Half-scale breadboard demonstrators for impact testing.

The mass of each one of the breadboards manufactured was measured and registered in Table .

Table 2 - Total mass of full and half-scale breadboards.

Full-Scale breadboard	Half-Scale (1) breadboard	Half-Scale (2) breadboard
22.40kg	3.19kg	3.16kg

In Fig. 18 are summarized the main dimensions for the full-scale breadboard including the COG (Centre of Gravity) position.

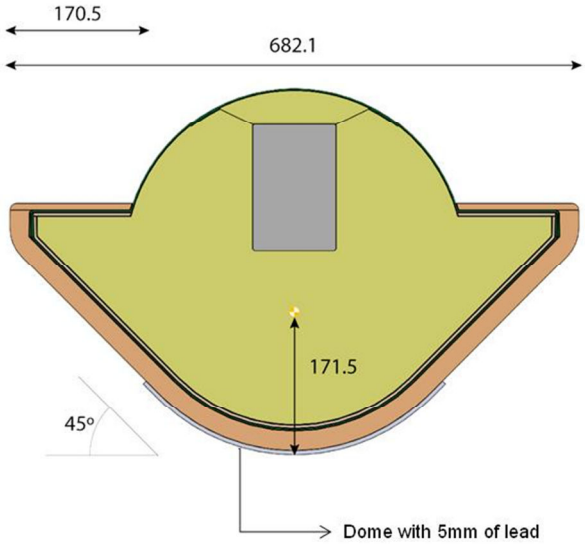

Fig. 18 - Full-scale breadboard dimensions and position of COG.

Drop-tests (Kinematic tests)

The breadboard drop-tests were achieved with the help of a special crane (see Fig. 19) that lift the breadboards to a maximum height equal to, approximately, 85m and 50m for the full and half-scales breadboards, respectively. An autonomous logger for measuring the container's deceleration, was accommodated inside the steel container. The breadboards impacted two different type of soils, namely, dense sand and tarmac. The site for impact against deformable soil was duly prepared considering an impact with 15m in diameter and 0.5m height of sand (sieve 4) mixed with gravel.

Fig. 19 - Crane used for breadboard drop-tests.

Thermal tests

The sensorisation of the breadboard for the thermal test considered the installation of 15 temperature sensors around the bio-container and at breadboards as seen in Fig. 20 and Fig. 21. A thermal loading profile was set ranging between 1 ºC and 80 ºC with an isothermal plateau at T=80 ºC, with 3.5 h of duration.

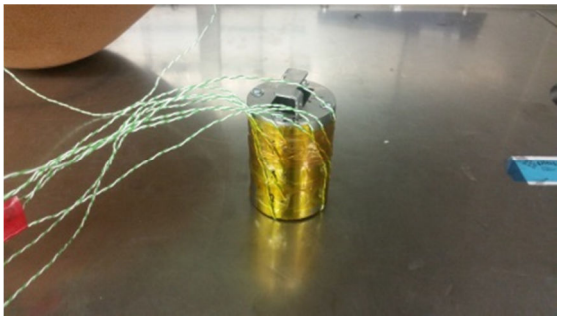

Fig. 20 - Thermopars positioned around the bio-container.

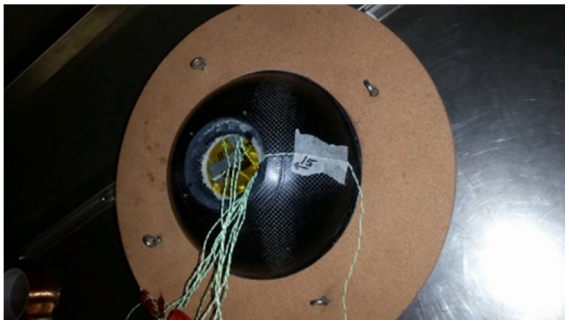

Fig. 21 - Temperatures sensors installed in the external surface of the breadboard.

RESULTS

Full-scale breadboard (Kinematic tests)

A successful drop was achieved for the full-scale breadboard as shown in Fig. 22. The full-scale breadboards were released from a height equal to, approximately, 85m achieving a terminal velocity equal to, approximately, 36ms^{-1}. The breadboard terminal velocity was obtained through the analysis of high-speed camera images.

Fig. 22 - Full-scale breadboard after impact.

After recovering the breadboard the top shell of the breadboard was opened finding that the bio-container maintained its structural integrity not evidencing any sign of permanent deformation. A 45º slice was extracted from the breadboard (see Fig. 23) and used for the most relevant measurements. From Fig. 23a) it is possible to see the stroke (h_s) suffered by the bio-container causing permanent deformation to the crushable material and the measurements taken after impact, reproduced in Table 3.

(a) (b)

Fig. 23 - In a) the section-cut of the full-scale breadboard (after impact) and in b) a 45º slice and respective measured variables.

Table 3 - Variable nomenclature and experimental measurements.

Variable	Meaning	Value (mm)
$\mathbf{h_c}$	Bio-container's height	150
$\mathbf{h_s}$	Bio-container's stroke	95
$\mathbf{h_r}$	Nose-tip stroke	110
$\mathbf{h_{rm}}$	Remaining crushable material	75
$\mathbf{h_t}$	Available stroke	205

Half-scale breadboard (Kinematic)

The half-scale breadboards were dropped-off from a height equal to approximately 51m achieving a terminal velocity equal to, approximately, 26ms^{-1}. Two different types of soil were considered for the impact of the half-scale breadboards: dense sand and tarmac as shown in Fig. 24.

Fig. 24 - Impact against: dense sand (left) and tarmac (right).

For the two half-scale breadboard's it was possible to monitor the bio-container's deceleration via the autonomous logger installed inside the bio-container. In Fig. 25 and Fig. 26is displayed the bio-container's deceleration components obtained for impact against tarmac (rigid soil) and dense sand, respectively. It should be noticed that the XX component of the acceleration logger is aligned with the direction of impact.

For the impact against rigid soil (Tarmac) the deceleration peak is obtained for the XX component with a value equal to, approximately, 1000g's. The other deceleration components are not meaningful in comparison with the axial (XX) component. The deceleration peak obtained for the impact against dense sand is inferior, corresponding to, approximately, 900g's. For this case in particular is also visible a rise in the deceleration values for the ZZ deceleration component resulting from a slight inclination of the ERC due to the soil irregularity at the impact site.

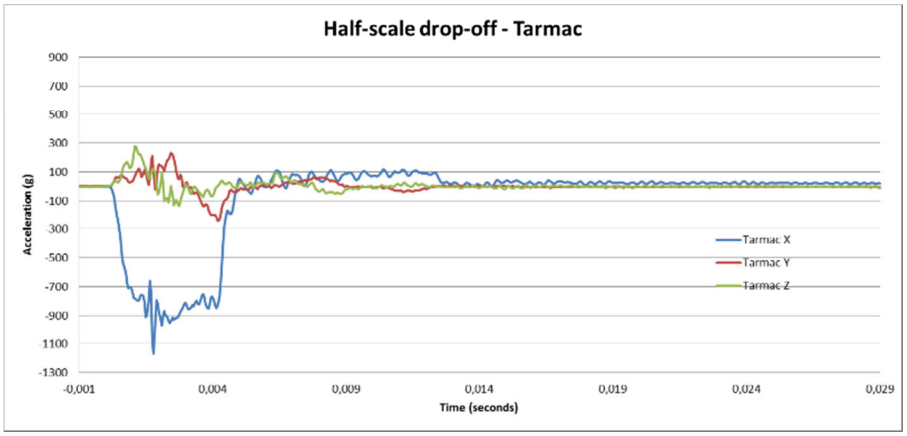

Fig. 25 - Bio-container's deceleration transient for half-scale breadboard impacting against tarmac.

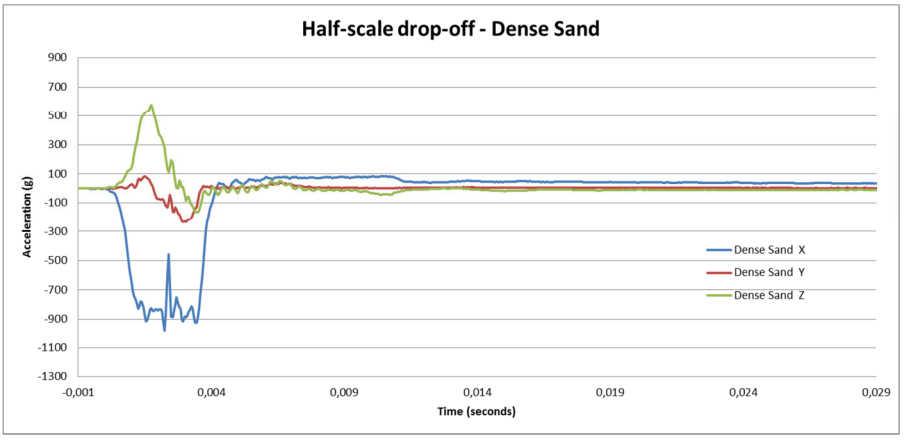

Fig. 26 - Bio-container's deceleration transient for half-scale breadboard impacting against dense sand.

Thermal Tests

Data in Fig. 27 compare the thermal behavior of the breadboard (half-scale) before and after impact, in order to quantify the dependence of the breadboard's thermal response with the permanent deformation of the crushable material. It is observable a slight change on the thermal response of the ERC after suffering impact.

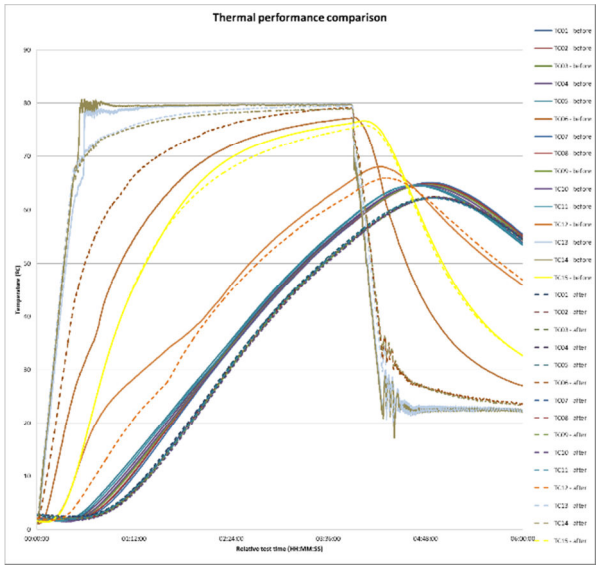

Fig. 27 - Thermal performance comparison: data before (continuous line) and after (dashed line) impact.

CORRELATION EXPERIMENTAL/NUMERICAL DATA

Full-scale breadboard (Kinematic)

Several correlations studies were performed in order to check the accuracy of the proposed numerical models, including the direct comparison of structural variables obtained from the 45º slice (see Fig. 23), such as bio-container's stroke and other relevant variables. Fig. 28, through the superposition of the deformed configurations obtained numerically an experimentally, resumes quite well the good agreement obtained between numerical and experimental data.

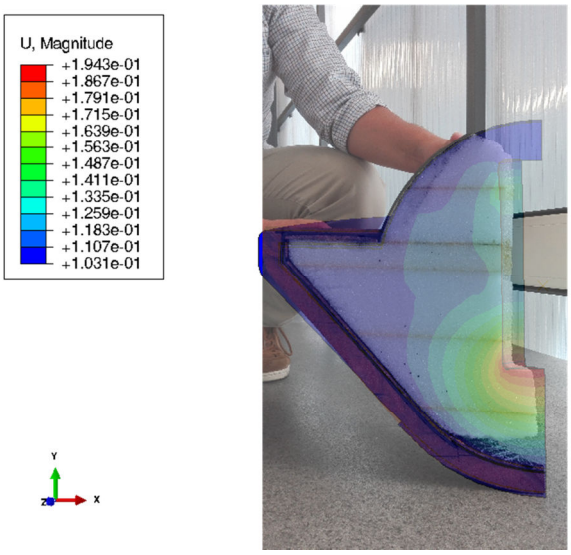

Fig. 28 - Visual comparison of simulated and experimental results (superposition of numerical and experimental results).

Table 4 - Measured variables and correlation with numerical results.

Variable	Experimental	Numerical	Relative error
h_s (mm)	95.0	87.4	8.6%
h_r (mm)	110.0	114.1	-3.6%
h_{rm} (mm)	75.0	79.7	-5.8%
Soil (mm)	140.0	133.4	4.9%

Half-scale breadboard (kinematic)

In Fig. 29 is depicted the comparison of deceleration transients obtained experimental and numerically, for an initial velocity set to approximately 26 ms^{-1}, in accordance with the velocity measured experimentally. Also, and for same impact velocity is shown in Fig. 30, the bio-container's deceleration transient obtained during the impact against dense sand.

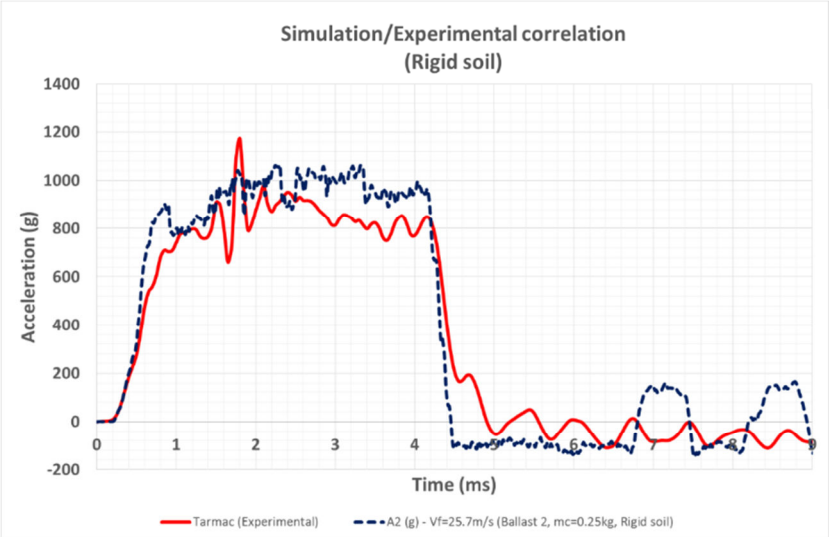

Fig. 29 - Bio-container's deceleration transient for impact against rigid soil.

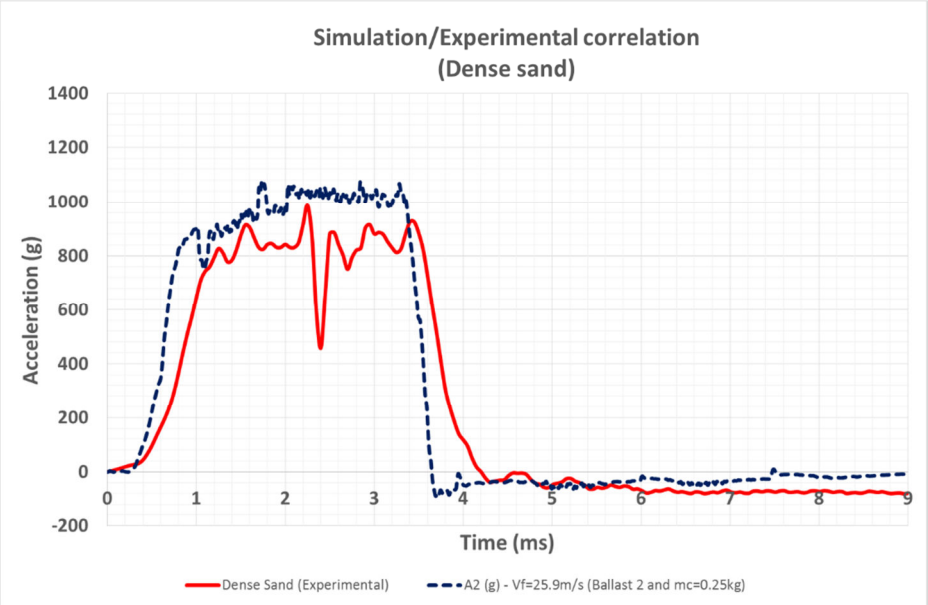

Fig. 30 - Bio-container's deceleration transient for impact against dense sand.

The experimental and numerical deceleration transients, for the different impact situations, compare quite well as can be observed in Fig. 29 and Fig. 30. In fact, both the deceleration peak values, the time duration of impact transient and the shape of the deceleration profile obtained numerically have a very good correlation with the deceleration results obtained experimentally.

Half-scale breadboard (thermal)

In Fig. 31 is shown the comparison between numerical and experimental thermal results obtained for six relevant temperature sensors considering convective heat transfer coefficients equal to h=50 $Wm^{-2}K^{-1}$. The temperature sensors nomenclature and respective positions are coherent to the reported experimentally.

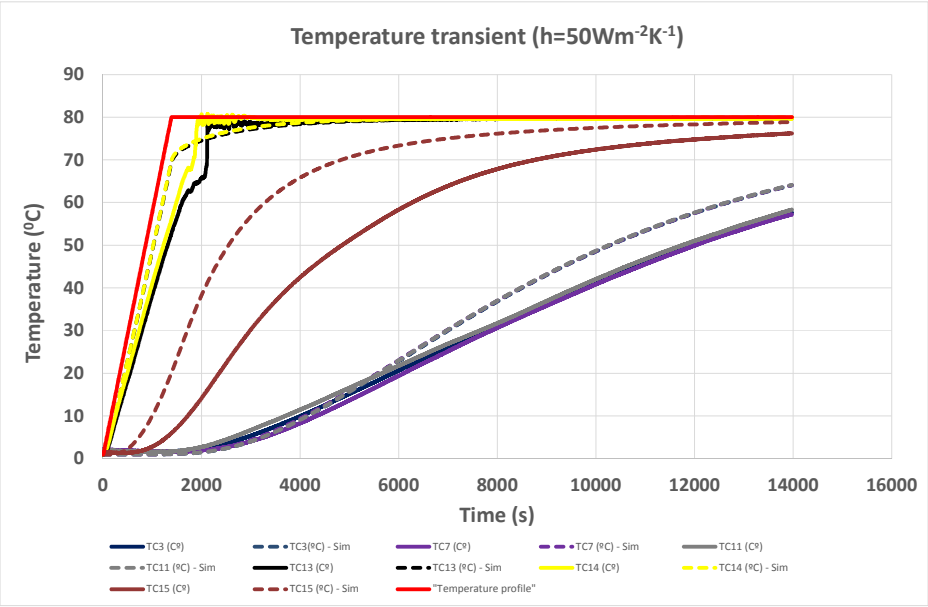

Fig. 31 - Comparison of numerical and experimental results for h=50$Wm^{-2}K^{-1}$.

The correlation obtained for the thermal tests is fairly good with some discrepancies in one of the thermopars considered (TC 15 is an example) due, possibly, to the difficulty in establishing a coherent relation between the real position of sensor TC15 (positioned inside the breadboard before the thermal test) and the coordinates of the monitored node in the numerical model.

CONCLUSIONS

The activities covered by the cTPS project have as a final result the design, manufacturing and test of a ERC capable of: 1) providing an adequate thermal response during atmospheric reentry, 2) maintaining the ERC's structural integrity while controlling the deceleration values at the bio-container during impact against both deformable and rigid soil and 3) maintaining the bio-container temperature bellow a specified temperature during a specific period of time, for the post-impact phase.

The design of the cTPS structure (for both the MSR and Phootprint missions) was supported by the intensive use of numerical techniques that, through the modelling of the thermomechanical behaviour of the cTPS systems proposed, allowed the design optimization of several design concepts for the ERC including aspects related with material selection procedures.

Material pre-selection tests were conducted and responsible for the selection of several potential materials for the cTPS system. The preselection was based on material data obtained from different bibliographical sources, producer data and preliminary tests performed by the consortium. In sequence, a detailed material characterization plan that included uniaxial tensile, uniaxial compression and shear tests with strain-rate and temperature dependence were performed. Also, thermal tests that included thermal conductivity (with permanent deformation dependence), specific heat and thermal expansion were led. The detailed characterization tests were performed on the pre-selected materials allowing a complete and coherent description of its thermomechanical capacities. Simultaneously, the material data served as an input to the calibration of constitutive models.

The cTPS concepts were tested in representative conditions through drop and forced thermal convection tests. The sensorisation scheme considered for the breadboard allowed the extraction of kinematic (bio-container's deceleration) and thermal data, used to, simultaneously, check the structural integrity of the breadboard (and bio-container) and correlation with data obtained from numerical models in order to check accessing its applicability.

As a final conclusion it can be stated that: 1) a valid cTPS concept (design and material selection) was proposed and duly tested, 2) thermomechanical data of several crushable materials were obtained and reported in detail, 3) thermomechanical numerical models that reproduce coherently the underlying physics of the different phenomena involved in an atmospheric re-entry process were made available and 4) experimental data concerning drop-tests and thermal tests confirm the adequacy of the design proposed and the quality of the results obtained numerically.

REFERENCES

[1]-ACC-Amorim Cork Composites. (2016). Corecork by Amorim. (ACC-Amorim Cork Composites) Retrieved 2016, from http://www.matrix-composites.co.uk/prod-data-sheet/cork/mds-gama-corecork.pdf

[2]-Evonik. (2016). ROHACELL® WF: first choice for aeronautic and aerospace applications. Retrieved 11 27, 2016, from: http://www.rohacell.com/product/rohacell/en/products-services/rohacell-wf/pages/default.aspx

[3]-Geothecnical Parameters. (n.d.). Retrieved 12 02, 2015, from Geotechdata.info: http://www.geotechdata.info/parameter/parameter.html

[4]-NASA. (2017, 01 24). Thermal Protection System (TPS) and Materials. Retrieved 01 24, 2017, from NASA: https://www.nasa.gov/centers/ames/research/humaninspace/humansinspace-thermalprotectionsystem.html

[5]-S, D. V., & Fleck, N. A. (2000). Isotropic Constitutive Model for Metallic Foams. Journal of the Mechanics and Physics of Solids, 48, 1253-1276.

[6]-Z, H. (1980). Failure Criteria for Unidirectional Fiber Composites. Journal of Applied